Nano Research

Open Access

Research Article

Precise size-matching of platinum nanoparticles in pyrene-based covalent organic frameworks for pH-universal hydrogen evolution

Jiahui Li[§], Chaoyu Zhao[§], Rong Chen, Yang Xiao, Shuo Han, Lin Lin ✉, Jialu Li ✉, and Xiaofei Jing ✉

Key Laboratory of Polyoxometalate and Reticular Material Chemistry of Ministry of Education, College of Chemistry, Northeast Normal University, Changchun 130024, China

[§] *Jiahui Li and Chaoyu Zhao contributed equally to this work.*

Cite this article: *Nano Research*, **2026**, *19*, 94909047. https://doi.org/10.26599/NR.2026.94909047

ABSTRACT: Hydrogen is a promising clean energy carrier, and electrocatalytic water splitting via the hydrogen evolution reaction (HER) represents a sustainable production strategy. While platinum nanoparticles (PtNPs) typically exhibit superior HER performance, their immobilization requires meticulous consideration due to an inherent aggregation tendency in solution. In this work, precise size-control of PtNPs was achieved by employing pyrene-based covalent organic frameworks (COFs) as effective hosts. Two COFs with similar mesoporous skeletons (IL-COF-2 and Azo-COF) and their sulfur-rich derivatives (TIL-COF-2 and TAzo-COF) were synthesized. These COFs feature ordered one-dimensional channels with diameters between 2.4 and 2.9 nm. Benefiting from the synergistic effects of spatial confinement and heteroatomic interactions, ultrafine PtNPs were uniformly immobilized within these COFs, with average particles sizes ranging from 1.7 to 1.9 nm. The resulting Pt@COFs all demonstrated excellent catalytic activities across a universal pH range, including acidic (0.5 M H_2SO_4), alkaline (1 M KOH) and neutral (1 M phosphate buffered saline (PBS)) media. Among them, the heteroatom-rich Pt@TAzo-COF exhibited the most outstanding HER performance. This study realizes the precise size-matching between PtNPs and COFs, providing a robust strategy for effective Pt immobilization and enhanced pH-universal HER efficiency.

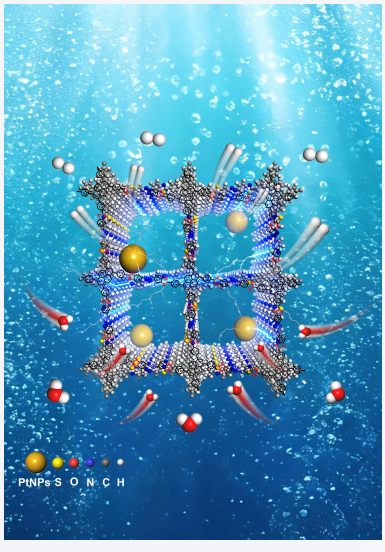

KEYWORDS: covalent organic frameworks (COFs), metal nanoparticles, heterogeneous catalysis, water splitting, green hydrogen

1 Introduction

Hydrogen is a clean and renewable energy carrier with a high calorific value, making it a viable alternative to fossil fuels and suitable for modern industrial production [1, 2]. Currently, methane steam reforming remains the dominant approach for industrial hydrogen production; however, it generates substantial CO_2 emissions, which conflicts with the objective of a low-carbon society [3–5]. Electrocatalytic water splitting serves as an alternative approach, where efficient electrocatalysts for hydrogen evolution reaction (HER) play a crucial role [6–8]. Among various metal catalysts [9], platinum (Pt) is an ideal HER electrocatalysts because of its high reactivity and optimal metal-hydrogen binding energy [10, 11]. It is well established that the catalytic activity of metals is closely related to their particle size, and smaller nanoparticles have superior efficiency compared to larger ones [12–15]. However, platinum nanoparticles (PtNPs) possess high surface energy, making them kinetically unstable during reactions and prone to aggregation in solutions [16]. This hinders the exposure of more catalytic active sites, thereby deteriorating their catalytic performance. Various support materials, especially porous materials with high surface areas, have been investigated for PtNPs immobilization [17–19]. Nevertheless, precise control of PtNPs with narrow size distributions on support materials remains a significant challenge, and developing effective immobilization strategies are highly desired.

Covalent organic frameworks (COFs) are a class of thermodynamically stable porous materials, which are constructed with strong covalent bonds and can serve as effective supports for PtNPs. Due to their predictable structures, COFs can also be designed and synthesized with abundant active sites to promote

Received: June 5, 2026; **Revised:** July 13, 2026
Accepted: July 21, 2026

✉Address correspondence to Xiaofei Jing, jingxf100@nenu.edu.cn; Jialu Li, lijl111@nenu.edu.cn; Lin Lin, linlin@nenu.edu.cn

HER through the synergistic effect between PtNPs and COFs' active sites [20–24]. Among these, two-dimensional COFs feature regular, interconnected one-dimensional channels that facilitate charge transfer and mass transport [25–27]. At the same time, COFs equipped with electronegative heteroatoms such as S, N, and P are considered as suitable support materials, because the presence of these heteroatoms can modulate electron cloud distribution and expedite electron transfer, thereby strengthening the interaction between PtNPs and COFs, and preventing them from large-scale agglomeration and leaching [28–31]. Consequently, multi-heteroatom engineering of two-dimensional COFs are promising strategies to obtain efficient heterogeneous Pt-based HER catalysts.

Generally, two-dimensional mesoporous COFs favor staggered (AB) rather than eclipsed (AA) stacking mode to minimize interlayer electrostatic repulsion [32]. However, AB stacking often create constricted channels that obstruct the deep diffusion of metal precursors and cause transport limitation [33–35]. Pyrene units with planar geometry and extensive delocalized π-system have a robust tendency to form stable, periodic π-columns via intense π–π stacking, and the stacked motifs will facilitate the formation of highly ordered COFs with AA stacking mode [36–38]. Therefore, pyrene-based COFs always have straight-through one-dimensional channels that ensure maximum accessibility and provide an ideal confined environment for the immobilization of ultrafine PtNPs.

In this work, two pyrene-based COFs (IL-COF-2 and Azo-COF) with similar mesoporous channels, along with their sulfur-rich derivatives (TIL-COF-2 and TAzo-COF) were synthesized for the precise size control of PtNPs. By rational framework engineering, these COFs show slightly tunable channel diameters ranging from 2.4 to 2.9 nm, as well as functional microenvironments with multi-heteroatoms such as nitrogen and sulfur. The synergistic effect of spatial confinement and multi-heteroatom interaction within these four COFs constrains the growth of PtNPs to an ultrafine scale of 1.7–1.9 nm. The resulting Pt@COFs all exhibit superior catalytic performance towards HER, among which the heteroatom-rich Pt@TAzo-COF demonstrated the best HER activity as a higher content of heteroatoms in COFs can produce Pt@COFs catalysts with higher Pt loading. Notably, these Pt@COFs show great pH-universal HER activity benefiting from the synergistic effect of electronic modulation induced by heteroatoms and spatial confinement of COF channels.

2 Experimental section

2.1 Chemicals and materials

2,6-Diaminonaphthalene, 1,2-dichlorobenzene (*o*-DCB), sulfur (S_8), and potassium tetrachloroplatinate(II) (K_2PtCl_4) were purchased from Energy Chemicals and Innochem. 4,4'-Azodianiline and 1,3,6,8-tetrakis(4-formylphenyl)pyrene (TFPPy) were purchased from Jilin Chinese Academy of Sciences - Yanshen Technology Co., Ltd. Carbon black and 5 wt.% Nafion were purchased from Acros Organic. All chemicals were used without further purification.

2.2 Characterization

Fourier transform infrared spectroscopy (FTIR) was collected by Nicolet Impact 410 Fourier transforms infrared spectrometer. Solid-state ^{13}C cross-polarization/magic angle spinning nuclear magnetic resonance (CP/MAS NMR) spectra were studied by Bruker Avance III model 400 MHz NMR spectrometer at a MAS rate of 5 kHz. Scanning electron microscopy (SEM) and transmission electron microscopy (TEM) images were recorded by field emission scanning electron microscopy (FE-SEM, SU-8010, Hitachi) and JEOL JEM-2100PLUS TEM at an accelerating voltage of 200 kV. Thermogravimetric analysis (TGA) was tested by a METTLER-TOLEDO TGA/DSC 3+ analyzer at a heating rate of 10 °C·min^{-1} in air atmosphere. Powder X-ray diffraction (PXRD) was performed on a Rigaku SmartLab X-ray diffractometer with Cu Kα radiation (40 kV, 30 mA, λ = 1.5418 Å) and at a scanning step of 0.01°. N_2 adsorption–desorption isotherms at 77 K were carried out on a Quantachrome Autosorb-iQ2 analyzer. X-ray photoelectron spectroscopy (XPS) was performed by an Escalab-MK II photoelectronic Spectrometer. The metal content was detected using inductively coupled plasma-atomic emission spectrometer (ICP-AES) on a LEEMAN Labs Prodigy.

2.3 Synthesis of IL-COF-2 and TIL-COF-2

20.4 mg of TFPPy (0.033 mmol) and 10.3 mg of 2,6-diaminonaphthalene (0.065 mmol) were added into a 10 mL vial. Subsequently, 0.1 mL of AcOH (6 M), 0.5 mL of 1,2-dichlorobenzene (*o*-DCB), and 0.5 mL of *n*-butanol (*n*-BuOH) were added to the vial. The mixture was sonicated for 5 min to ensure a uniform dispersion of the reactants. Following this, the vial was immersed in a liquid nitrogen bath to rapidly cool the contents, and then subjected to vacuum evacuation for 20 min prior to flame sealing. The sealed vial was allowed to cool to room temperature before being heated at 120 °C for a period of 3 d to facilitate the reaction. After reaction, the precipitate was collected via filtration and washed exhaustively with methanol (3 × 50 mL) and tetrahydrofuran (3 × 50 mL) to remove any residual reactants. Further purification of the product was achieved through a Soxhlet extraction process, utilizing methanol and tetrahydrofuran as solvents over a period of 2 days. The final step involved drying the product under vacuum at 90 °C for 12 h, resulting in the formation of a brownish-yellow powder with an overall yield of 89%.

The synthesis of TIL-COF-2 was conducted by introducing 20.4 mg of TFPPy (0.033 mmol), 10.3 mg of 2,6-diaminonaphthalene (0.065 mmol), and 12.5 mg of sulfur (0.39 mmol) into a 10 mL vial. Subsequently, 0.1 mL of AcOH (6 M), 0.45 mL of *o*-DCB, 0.5 mL of *n*-BuOH, and 0.05 mL of DMSO were added to the vial. The subsequent experimental procedure was the same as that described above, resulting in a brown powder with a yield of 85% (Fig. S1 in the Electronic Supplementary Material (ESM)).

2.4 Synthesis of Azo-COF and TAzo-COF

The synthesis of Azo-COF commenced with the introduction of 12.4 mg of TFPPy (0.02 mmol) and 8.5 mg of 4,4'-azodianiline (0.04 mmol) into a 5 mL ampoule. Subsequently, 2 mL of *o*-DCB and 0.2 mL of AcOH (6 M) were added to the ampoule. The mixture was sonicated for 10 min to achieve a homogeneous dispersoid. The ampoule was then cooled to 77 K in liquid nitrogen, evacuated for 5 min, and allowed to thaw under nitrogen protection. This cooling and evacuation process was repeated three times. Following the final thawing, the ampoule was sealed under vacuum and returned to room temperature before being placed in a 120 °C oven for a period of 3 d to complete the reaction. Upon completion, the precipitate was collected by filtration and washed exhaustively with methanol (3 × 50 mL) and THF (3 × 50 mL) to remove any unreacted reactants. The product was further purified

using Soxhlet extraction with methanol and THF as solvents over a period of 2 days. The final step involved drying the product at 90 °C for 12 h, yielding a brownish-yellow powder with a yield of 76%.

For the synthesis of TAzo-COF, 12.4 mg of TFPPy (0.02 mmol), 8.5 mg of 4,4'-azodianiline (0.02 mmol), and 6.4 mg of sulfur (0.2 mmol) were added into a 10 mL ampoule. Then, 0.1 mL of DMSO, 2 mL of *o*-DCB, and 0.2 mL of AcOH (6 M) were added to the reaction mixture. The subsequent experimental steps were the same as those described above, resulting in a brown powder with a yield of 63% (Fig. S2 in the ESM).

2.5 Synthesis of Pt@Azo-COF, Pt@TAzo-COF, Pt@IL-COF-2 and Pt@TIL-COF-2

Taking Pt@Azo-COF as an example: 25 mg of Azo-COF was dispersed in 20 mL of methanol and sonicated for 30 min to achieve a uniform dispersoid. With vigorous stirring, 1 mL of K_2PtCl_4 aqueous solution (5 mg·mL^{-1}) was slowly added to the system. The mixture was then stirred continuously at room temperature for an additional 2 h to ensure thorough mixing. Subsequently, the reaction mixture was heated to 65 °C for 5 h. After the reaction was completed, the solid product was collected by filtration and washed three times with a mixture of ethanol and acetone in a volume ratio of 1:8. Finally, the product was dried under vacuum at 60 °C for 12 h, yielding a dark brown Pt@Azo-COF composite (Fig. S3 in the ESM).

2.6 Electrochemical measurements for HER

The electrochemical measurements of as-synthesized catalysts were tested by CHI660 electrochemical workstation. A three-electrode system was used including an Ag/AgCl (saturated KCl) electrode as a reference electrode, a carbon rod as a counter electrode and nickel foam (NF) as the working electrode. The reversible hydrogen electrode (RHE) was obtained by the equation: $E_{(RHE)} = E_{(Ag/AgCl)} + 0.095\ pH + 0.197\ V$. To eliminate the effect of electrolyte resistance, all polarization curves were corrected with 0.9*iR* and conducted at room temperature.

2.7 Preparation of working electrodes with Pt@COFs

7 mg as-prepared catalyst and 3 mg carbon black were dispersed in a mixture with 50 μL of Nafion solution (5 wt.%) and 450 μL of ethanol solution, then the mixture was sonicated for 30 min below 30 °C. The 80 μL of homogeneous catalyst ink was slowly dropped onto a 1 cm × 0.8 cm of NF and dried under room temperature.

2.8 Theoretical calculation

All theoretical calculations were performed with the Vienna *ab-initio* simulation package (VASP) [39, 40]. Projector augmented-wave (PAW) pseudopotentials and the generalized gradient approximation (GGA) with the Perdew–Burke–Ernzerfhof (PBE) functionals were used to treat the electron–ion interactions and the exchange-correlation interaction between electrons, respectively [41]. Additionally, the Grimme method (DFT-D3) was incorporated to take into account the weak van der Waals interactions [42]. The valence electron wave functions were described by a plane wave basis set that was set to 500 eV. The convergence thresholds for geometry optimizations were 10^{-5} eV and 0.05 eV·Å^{-1} for total energy and ionic force, respectively. A gamma-centered Monkhorst-Pack scheme was used to sample a 2 × 2 × 1 *k*-points grid for describing the Brillouin zone in the reciprocal space. The climbing-image nudged elastic band (CI-NEB) method was employed to identify the transition state (TS) structure [43]. A vacuum layer of over 15 Å was maintained along the *z*-axis to preclude neighboring layer interactions. The Gibbs-free energy (ΔG) changes are calculated by $\Delta G = \Delta E + \Delta ZPE - T \times \Delta S$, where ΔE, ΔZPE, T, and ΔS are electronic energy difference, zero-point energy change, temperature, and entropy change, respectively. The free energy of hydrogen was referenced to the energy of $1/2H_2$ at standard conditions.

3 Results and discussion

Under solvothermal conditions, four pyrene-based COFs (IL-COF-2, Azo-COF, TIL-COF-2 and TAzo-COF) with AA stacking mode were selected and synthesized by employing TFPPy as the effective building block (Fig. 1(a), Figs. S1 and S2 in the ESM). Ultrafine PtNPs were immobilized in these COFs via a post-synthetic approach to obtain related Pt@COFs (Fig. S3 in the ESM).

To confirm the successful polymerization and bonding features, FTIR of these COFs and corresponding monomers were recorded (Fig. S4 in the ESM). The disappearance of N–H stretching vibration at 3390 cm^{-1} and concomitant appearance of C=N characteristic peak at 1622 cm^{-1} proved completed Schiff base reaction. No significant changes were observed in the FTIR spectra of Pt@COFs compared with the pristine COFs, suggesting that the covalent skeletons remained intact upon PtNPs loading, which confirms the superior stability of the host materials. The chemical shifts for carbon atoms were all assigned accordingly in the solid-state ^{13}C CP/MAR NMR spectra (Fig. S5 in the ESM). The signal at 157 ppm is attributed to the carbon atoms in newly formed imine bonds (C=N) in IL-COF-2 and Azo-COF. The S–C=N bonds in thiazole rings are found at 167 ppm in sulfur-rich COFs, proving the successful incorporation of sulfur atoms into the frameworks. Elemental analysis reveals that the elemental contents in these COFs are consistent with theoretical values (Table S1 in the ESM).

The crystalline structures of these pyrene-based COFs were then verified by PXRD together with structural simulation. As shown in Fig. 1(b), the experimental diffraction patterns (blue curves) of these four COFs all fit well with the ones of simulated AA stacking models (red curves) rather than AB stacking models (black curves). The planar geometry and delocalized π-system of pyrene-based building blocks drive a strong inclination toward the assembly of stable periodic π-columns, thereby facilitating the crystallization of COFs with consistent AA stacking mode and straight-through one-dimensional channels. According to the simulated AA stacking models, the theoretical channel diameters are 2.50 and 2.82 nm for IL-COF-2 and Azo-COF. By rationally tuning the length of linkages, slightly regulated channel sizes in COFs were realized. After introducing sulfur atom to form thiazole rings, their channel sizes decreased to 2.43 and 2.74 nm for TIL-COF-2 and TAzo-COF, respectively. Although PXRD patterns of Pt@COFs showed slight intensity decreases, Pt@COFs demonstrated excellent crystallinity (purple curves) without distinct signals for PtNPs lattice. In the magnified PXRD patterns of Pt@COFs (Fig. S6 in the ESM), two diffraction peaks at 39.7° and 46.3° belonging to the Pt (111) and Pt (200) crystal planes were observed with weak intensities. This proves that ultrafine PtNPs were successfully immobilized in these pyrene-based COFs.

The morphology and microstructure of these pyrene-based COFs and their relevant Pt@COFs were studied with SEM and TEM. All COFs have a micrometer-scale rod-like morphology in their SEM images (Fig. S7 in the ESM), and the incorporation of

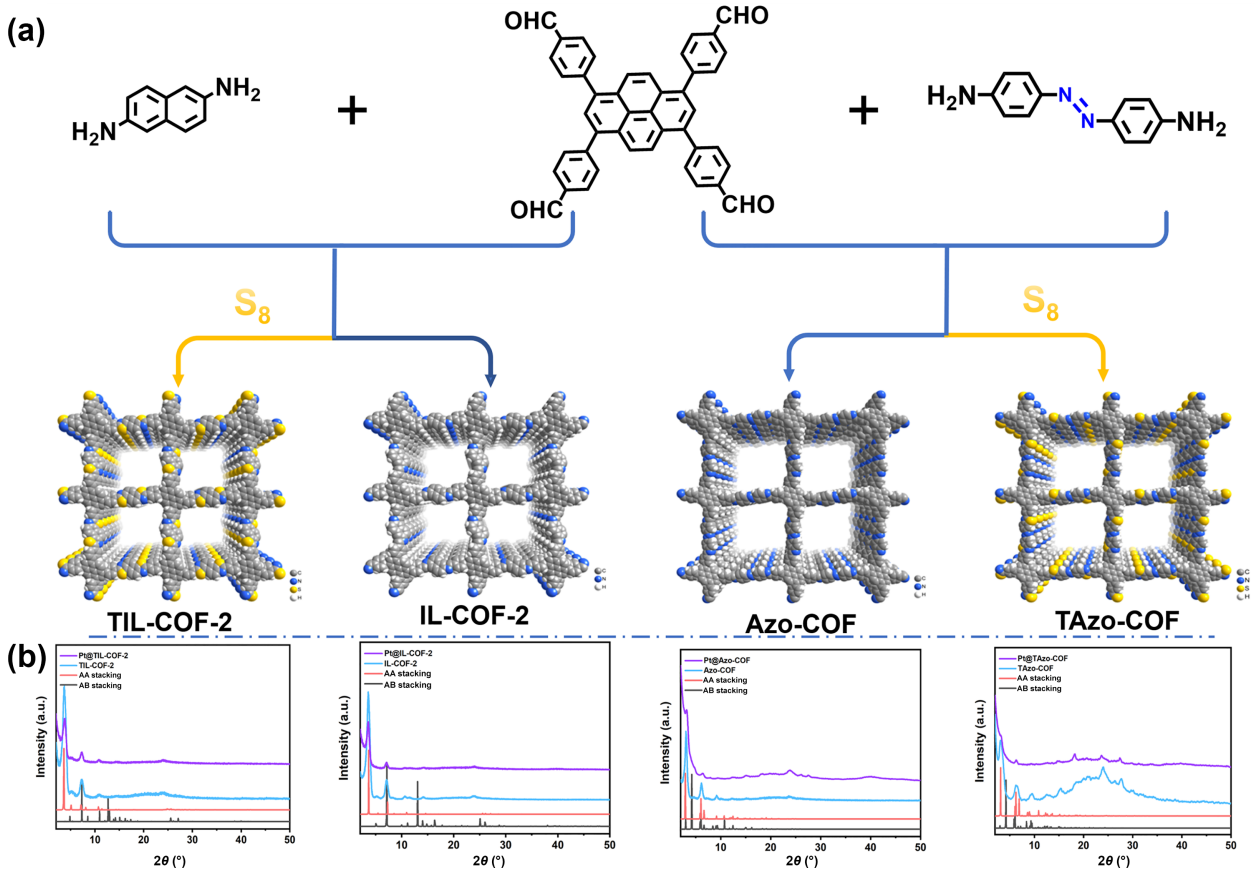

Figure 1 (a) Synthetic routes of IL-COF-2, Azo-COF, TIL-COF-2, and TAzo-COF. (b) PXRD patterns of COFs, Pt@COFs, and simulated diffraction profiles for the AA and AB stacking models.

PtNPs didn't affect their morphologies. SEM-EDS element mapping images reveal a uniform distribution of elements including C, N, S and Pt throughout these materials (Fig. S8 in the ESM). In the comparison of TEM images (Figs. 2(a)–2(d)), it is clearly shown that ultrafine PtNPs are well dispersed in these COFs without significant agglomeration. Majority of PtNPs have a particle size smaller than the theoretical pore size of COFs (Figs. 2(e)–2(h)). The average sizes of PtNPs in Pt@IL-COF-2 and Pt@Azo-COF are 1.74 and 1.83 nm (Figs. 2(i)–2(l)), while 1.87 and 1.89 nm for Pt@TIL-COF-2 and Pt@TAzo-COF, respectively. It is found that PtNPs tend to aggregate more readily around nitrogen and sulfur sites in sulfur-rich COFs, inducing slightly larger particle sizes. To further verify the crystalline structure of the confined PtNPs, high-resolution TEM (HRTEM) was performed, and clear lattice fringes of PtNPs were observed in all four Pt@COFs (Fig. S9 in the ESM). The measured interplanar spacings of 0.227 and 0.196 nm can be assigned to the Pt (111) and Pt (200) crystal planes, respectively, which are consistent with face-centered cubic Pt. The spatial confinement imposed by the well-defined one-dimensional channels of these pyrene-based COFs and heteroatomic synergistic effect have governed the nucleation and growth of metal species, and produced ultrafine PtNPs with narrow size distributions.

In order to verify the valence states of Pt species immobilized in pyrene-based COFs, XPS was conducted, and the signals of Pt 4f region confirm the presence of PtNPs (Fig. S10 in the ESM). The Pt 4f regions in all Pt@COFs exhibit a doublet with a low energy band ($4f_{7/2}$) and a high energy band ($4f_{5/2}$), with the values of 71.79–71.99 eV for Pt $4f_{7/2}$ and 75.05–75.13 eV for Pt $4f_{5/2}$, respectively. The slight variations in Pt binding energy are due to the local chemical environmental differences. These results demonstrate that Pt species have been successfully reduced from a divalent to a zero-valent state via the thermal reduction process mediated by methanol. The porous structures of these pyrene-based COFs and their corresponding Pt@COFs were then fully investigated to confirm the size-matching effect arising from the synergy between one-dimensional channels and heteroatom-functional frameworks. From N_2 adsorption–desorption isotherms measured at 77 K (Fig. S11 in the ESM), the specific surface areas of IL-COF-2 and Azo-COF were calculated to be 1576 and 1378 $m^2 \cdot g^{-1}$ using the Brunauer–Emmett–Teller (BET) model, while the BET surface areas are 458 and 242 $m^2 \cdot g^{-1}$ for TIL-COF-2 and TAzo-COF, respectively. During the synthesis of sulfur-rich COFs, bulky S_8 molecules were directly added into the reaction system to facilitate the *in-situ* formation of thiazole rings within the framework, thus leading to a concomitant reduction in the specific surface area. According to non-local density functional theory (NLDFT), the pore size distributions of pyrene-based COFs were calculated to be 2.35, 2.79, 2.43, and 2.21 nm, respectively, in good agreement with the previous theoretical simulation results (Fig. S12 in the ESM). Sulfur-rich COFs have a little broader pore distributions due to the introduction of bulky S_8 molecules in the synthetic systems. After immobilizing PtNPs, both the BET surface areas and pore sizes of Pt@COFs significantly decreased as expected. The BET surface areas are 584, 265, 565, and 161 $m^2 \cdot g^{-1}$, while the pore size distributions are 1.41, 1.67, 1.83, and 1.68 nm for Pt@IL-COF-2,

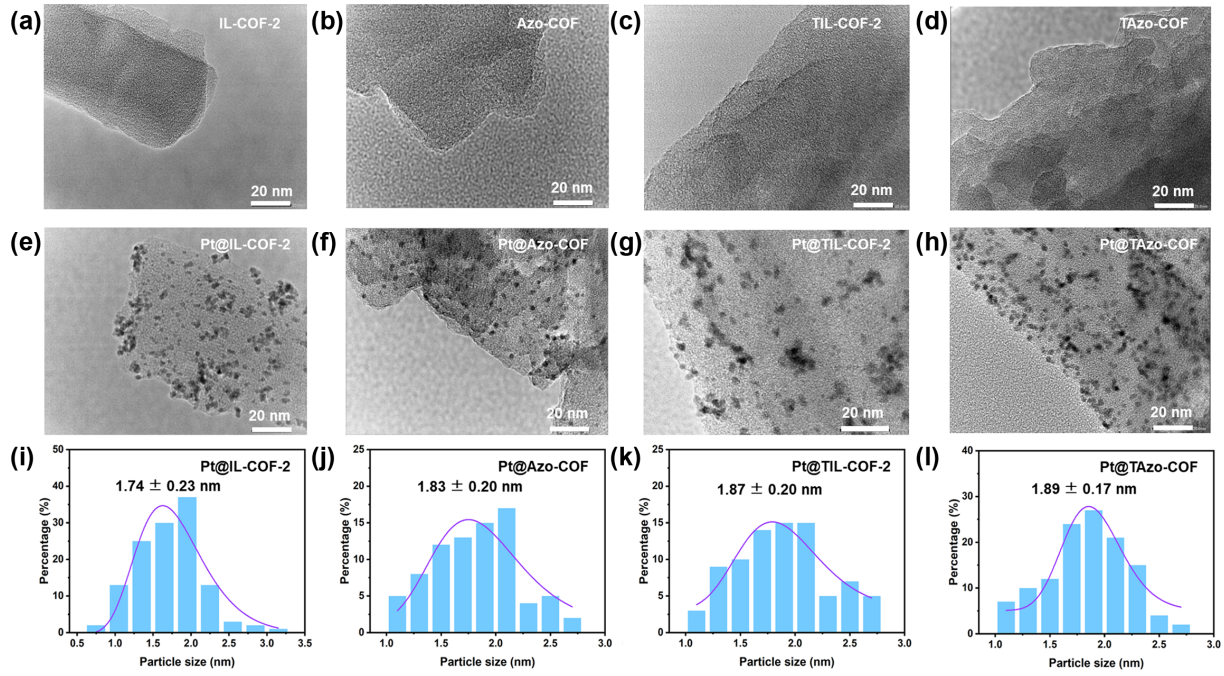

Figure 2 TEM images of synthesized COFs ((a) IL-COF-2, (b) Azo-COF, (c) TIL-COF-2, and (d) TAzo-COF) and Pt@ COFs ((e) Pt@IL-COF-2, (f) Pt@Azo-COF, (g) Pt@TIL-COF-2, and (h) Pt@TAzo-COF). (i)–(l) The pore size distributions of PtNPs within Pt@COFs.

Pt@Azo-COF, Pt@TIL-COF-2, and Pt@TAzo-COF, respectively. This provides direct evidence for the successful encapsulation of PtNPs within the COF channels. The high specific surface areas and narrow pore size distributions of the host COFs are conducive to precisely regulating the growth of metal nanoparticles, thereby ensuring a more uniform and well-defined Pt particle size distribution.

Stability is a crucial factor in evaluating materials' practical application. As shown in TGA, pyrene-based COFs are stable up to 300 °C, while the Pt@COFs started to decompose at a lower temperature (Fig. S13 in the ESM). By calculating the difference in the residual weight between COFs and Pt@COFs, the values were found to be 4.93%, 6.11%, 7.89%, and 9.67% for Pt@IL-COF-2, Pt@Azo-COF, Pt@TIL-COF-2, and Pt@TAzo-COF, respectively, which correspond approximately to the loading amounts of PtNPs. These results are consistent with the Pt contents measured by inductively coupled plasma (ICP), which are 4.62%, 6.53%, 7.42%, and 8.68% accordingly (Table S2 in the ESM). The Pt loading capacity are higher in the sulfur-rich COFs compared to IL-COF-2 and Azo-COF. This is benefited from the introduction of sulfur atoms, which provide a stronger affinity and enhanced interaction with Pt species. Furthermore, all COFs exhibit great stability in methanol, acetonitrile and alkaline solution (1 M KOH). After soaking in these solvents for over 24 h, these COFs still have good crystallinity (Fig. S14 in the ESM).

The above findings confirm the successful immobilization of ultrafine PtNPs within these pyrene-based COFs, where the one-dimensional channels have played a pivotal role in achieving size-matched encapsulation. Besides, the inherent thermal and chemical stability of these COFs underscores their potential for practical applications. Consequently, the HER performance of these Pt@COFs was systematically evaluated using a standard three-electrode system across a broad pH range, encompassing 0.5 M H_2SO_4 (acidic), 1 M KOH (alkaline) and 1 M phosphate buffered saline (PBS) (neutral) media. The electrodes were prepared by coating he pyrene-based COFs and Pt@COFs powders on nickel foam (NF). Then the *iR*-corrected linear sweep voltammetry (LSV) curves of these electrodes were collected at a scan rate of 10 mV·s^{-1}, and bare NF was employed for comparison. As shown in Fig. 3(a), the overpotential of bare NF, IL-COF-2, Azo-COF, TIL-COF-2, and TAzo-COF were recorded as 267, 248, 244, 226, and 195 mV (vs. RHE) to achieve a current density of 10 mA·cm^{-2} in the acidic system, indicating that pristine COFs do not possess HER electrocatalytic activity. After PtNPs encapsulation, the electrocatalytic activity of Pt@COFs significantly improved, the overpotentials of Pt@IL-COF-2, Pt@Azo-COF, Pt@TIL-COF-2, and Pt@TAzo-COF electrodes were 122, 115, 81, and 64 mV at 10 mA·cm^{-2}, respectively. In these Pt@COFs, PtNPs are highly dispersed with average particle sizes ranging from 1.74 to 1.89 nm. Given such marginal variations in nanoparticle size, the Pt loading content emerges as the more determinative factor in governing their HER catalytic activity. To assess the electrocatalytic kinetics of these electrodes, Tafel slopes for all materials were calculated from LSV curves (Fig. 3(b)). Pt@TAzo-COF with the highest Pt loading has the smallest Tafel slope (87 mV·dec^{-1}) compared to others, implying the fastest HER kinetics. Furthermore, the electrocatalytic active surface area (ECSA), which is directly proportional to the double-layer capacitance (C_{dl}) derived from cyclic voltammetry (CV) measurements (Fig. S15 in the ESM), was employed as a key criterion to quantify the density of active sites during the HER process. As shown in Fig. 3(c), Pt@TAzo-COF ($2C_{dl}$ = 2.4 mF·cm^{-2}) has the largest ECSA than other Pt@COFs. The Nyquist plots of electrochemical impedance spectroscopy (EIS) measurements were then conducted and the diameter of semicircle in EIS represented the charge transfer resistance (R_{ct}) at the electrode–electrolyte interface. Compared to the pristine COFs (Fig. 3(d)), all Pt@COFs have smaller R_{ct} value (Fig. 3(e)), and the resistance order for Pt@COFs was found to be: Pt@TAzo-COF < Pt@TIL-COF-2 < Pt@Azo-COF < Pt@IL-COF-2, reflecting the lowest charge-transfer resistance of Pt@TAzo-COF with highest Pt loading which facilitate

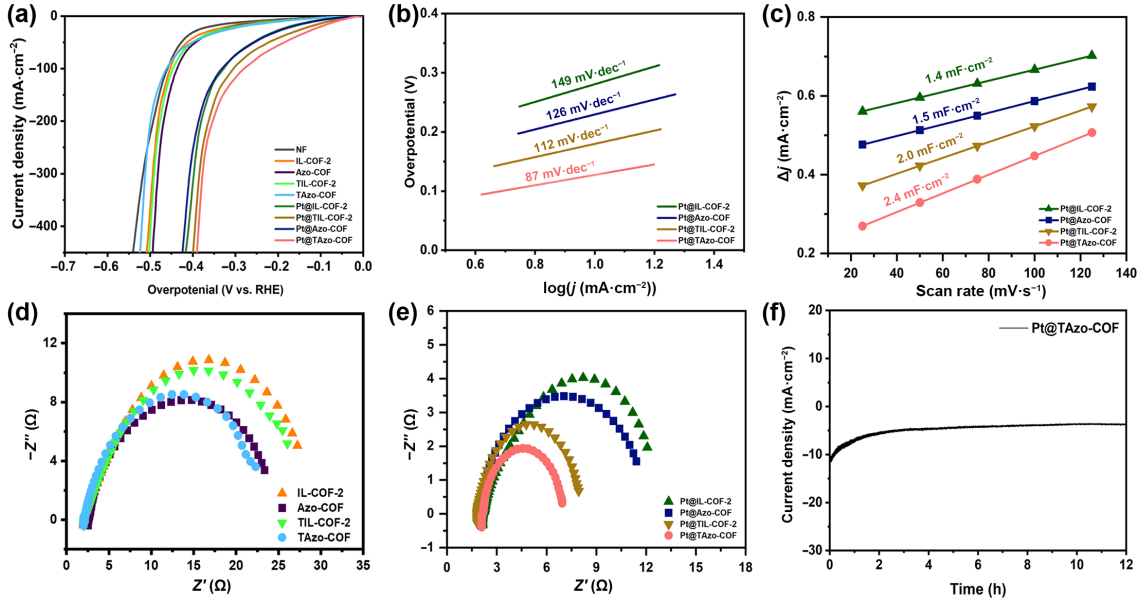

Figure 3 (a) LSV curves of NF, COFs, and Pt@COFs. (b) Tafel slopes and (c) the C_{dl} values of Pt@COFs in 0.5 M H_2SO_4 solution. The EIS Nyquist plots of (d) synthesized COFs and (e) Pt@COFs in 0.5 M H_2SO_4 solution. (f) *I*–*t* curves of Pt@TAzo-COF in 0.5 M H_2SO_4 media.

the charge transfer process. Additionally, the durability of Pt@TAzo-COF electrode was evaluated and it maintained a stable current density of 10 mA·cm^{-2} for 12 h in 0.5 M H_2SO_4 electrolyte (Fig. 3(f)). To further evaluate the catalytic performance compared to commercial Pt catalyst and cycling stability of Pt@TAzo-COF, two other electrodes with commercial Pt/C loaded on nickel foam (Pt/C/NF) and unsupported PtNPs loaded on nickel foam (PtNPs/NF) were prepared and tested under the same conditions in 0.5 M H_2SO_4 solution. As shown in Fig. S16 in the ESM, Pt@TAzo-COF exhibited comparable electrocatalytic performance with Pt/C/NF. The LSV curves of Pt@TAzo-COF before and after 2000 CV cycles show only a slight shift, indicating good cycling stability. In comparison, Pt/C/NF exhibits a more obvious activity decay after 2000 cycles, while PtNPs/NF undergoes a pronounced degradation despite its high initial activity. These results suggest that the COF framework contributes to the improved cycling stability of PtNPs during HER operation.

The electrocatalytic activities of Pt@COFs in the alkaline medium (1 M KOH) were then investigated, revealing a trend consistent with that observed under acidic conditions. Pt@TAzo-COF exhibits an overpotential of 86 mV at 10 mA·cm^{-2}, significantly outperforming Pt@IL-COF-2 (158 mV), Pt@Azo-COF (143 mV) and Pt@TIL-COF-2 (99 mV) (Fig. S17 in the ESM). Pt@TAzo-COF also displays a relatively low Tafel slope of 108 mV·dec^{-1} (Fig. S18 in the ESM), the largest ECSA ($2C_{dl}$ = 15.4 mF·cm^{-2}, Figs. S19 and S20 in the ESM) and the lowest charge-transfer resistance (Fig. S21 in the ESM). Moreover, the structural integrity of pyrene-based COFs ensures excellent long-term stability. Pt@TAzo-COF showed only negligible decay over 12 h of continuous chronopotentiometry in the alkaline electrolyte (Fig. S22 in the ESM). This pH-universal efficiency can also extend to neutral media (1 M PBS), where Pt@COFs maintain their superior catalytic activity and robust stability (Figs. S23–S28 in the ESM).

From the above results, it is seen that despite possessing lower specific surface areas than the pristine frameworks, the sulfur-rich COFs provide a higher density of anchoring sites, leading to significantly increased Pt loading. Consequently, the resulting Pt@COFs exhibit superior electrocatalytic activity toward HER, underscoring that the abundance of active sites outweighs the reduction in surface area. Among these Pt@COFs, the multi-heteroatomic skeleton of TAzo-COF seems provide the best confinement effect for Pt immobilization, therefore Pt@TAzo-COF demonstrated the highest Pt loading and outperforming catalytic activity.

To fully elucidate the reaction mechanism, structural models of Pt@Azo-COF and Pt@TAzo-COF were constructed (Fig. S29 in the ESM) and subjected to theoretical calculations. A series of density functional theory (DFT) calculations for the water dissociation process catalyzed by Pt@Azo-COF and Pt@TAzo-COF were performed, where Pt/N=N, Pt/N=C and Pt/N,S–C interaction sites were evaluated respectively. The charge density differences on these sites are denoted with decrease in electron density (cyan regions) and increase in electron density (yellow regions) in Fig. 4(a). Notably, the electron density distribution undergoes a pronounced change at the Pt/N,S–C interface, and evident electron accumulation is found around Pt species. This observation supports the hypothesis that the introduction of sulfur atoms enhances the interaction between metal center and COFs, facilitating rapid electron transfer at the interface and consequently improving catalytic performance. During the water dissociation process, water molecules are first adsorbed on the surface of catalysts, then dissociated to OH* and H* intermediates catalyzed by Pt and followed by the recombination of two H* to form H_2 molecule. The binding energies of reaction species on Pt/N=N, Pt/N=C and Pt/N,S–C interfaces for these three steps were calculated accordingly (Figs. S30–S32 in the ESM). As shown in Fig. 4(b), the binding energy absolute value of water molecule on Pt/N,S–C site is significantly larger (−4.38 eV) than those on Pt/N=C (−3.17 eV) and Pt/N=N (−2.84 eV), indicating that sulfur incorporation has effectively enhanced the interaction of COFs towards active species, leading to improved intrinsic activity and stability of PtNPs. Pt/N,S–C site in Pt@TAzo-COF also demonstrated the lowest energy barrier for water dissociation (0.41 eV), compared to 0.48

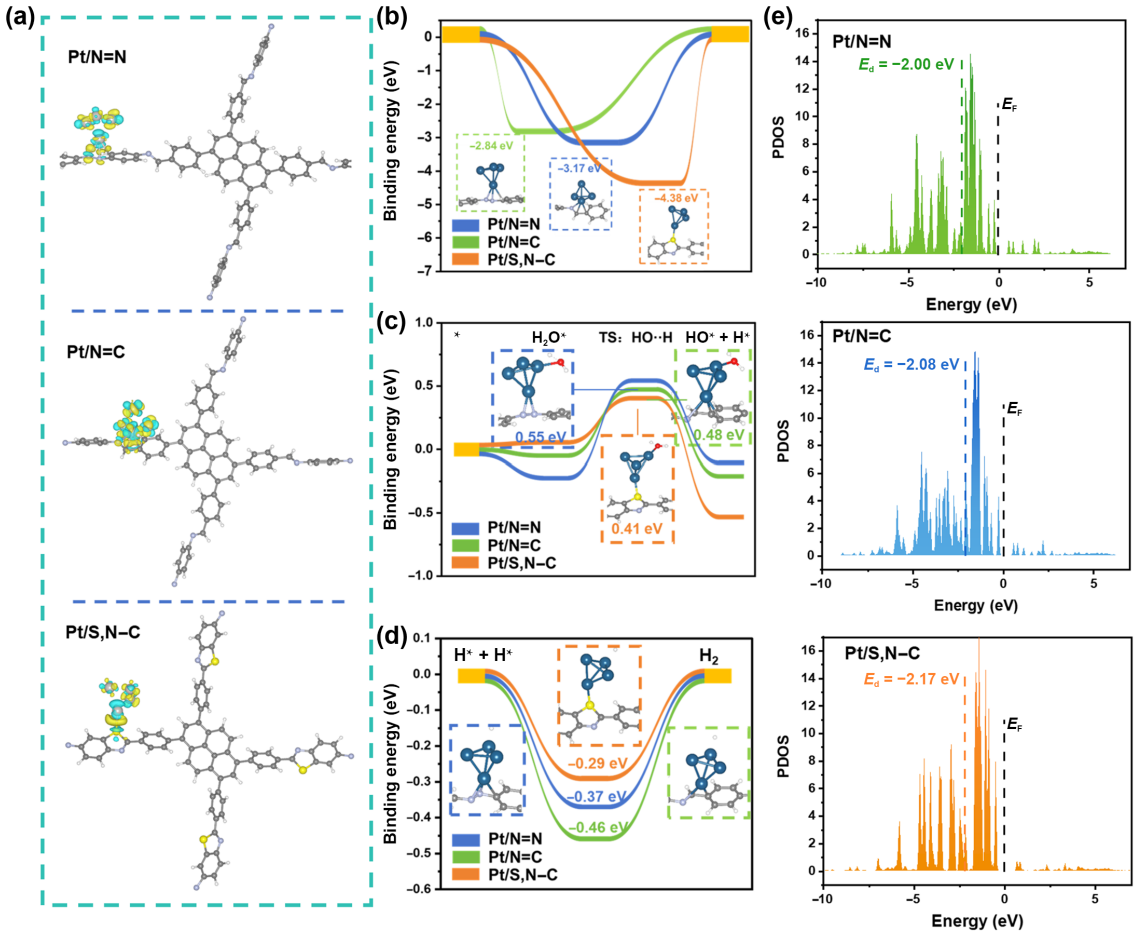

Figure 4 (a) The charge density difference images of Pt/N=N, Pt/N=C and Pt/S,N–C in Pt@COFs. Cyan areas represent reduced electron cloud density, while yellow areas indicate increased electron cloud density. The isosurface value is set to be 0.01 e·Å^{-1}. (b) Binding energies for support (N=N, N=C and S,N–C) with Pt. (c) Gibbs free energies for H_2O-adsorption/dissociation and (d) ΔG_{H^*} values calculated for Pt/N=N, Pt/N=C and Pt/S, N–C models in Pt@COFs. (e) PDOS results of Pt atoms for Pt/N=N, Pt/N=C, and Pt/S,N–C.

eV for Pt/N=C and 0.55 eV for Pt/N=N (Fig. 4(c)), indicating that the dissociation of water is promoted by Pt/N,S–C interface, consistent with electrochemical performances. According to the Sabatier principle, an optimal HER catalyst should exhibit a balanced binding strength with H* with low Gibbs free energy of hydrogen adsorption (ΔG_{H^*}). Indicated by Fig. 4(d), Pt/N,S–C site exhibits a more favorable ΔG_{H^*} value (−0.29 eV) compared to Pt/N=C (−0.37 eV) and Pt/N=N (−0.46 eV), thereby promoting H_2 generation and desorption in Pt@TAzo-COF catalyst. In addition, projected density of states (PDOS) analysis indicates that the d-band centers of Pt atoms on all sites are positioned at a lower energy level relative to the Fermi level (Fig. 4(e) and Fig. S33 in the ESM), which will facilitate H* desorption and optimize the hydrogen binding energy. This dual-functionalized surface not only provides strong anchoring sites to prevent the aggregation of ultrafine PtNPs through precise size-matching and chemical bonding but also optimizes the electronic structure of the active sites for pH-universal HER.

4 Conclusion

In summary, we have demonstrated a size-matching strategy for PtNPs immobilization within pyrene-based COFs featured with highly ordered one-dimensional mesoporous channels and heteroatom-functionalized skeletons. Leveraging the synergy effects of spatial confinement and heteroatomic interactions, ultrafine PtNPs were precisely confined within the COF nanochannels with exceptionally narrow size distributions from 1.74 to 1.89 nm. The resulting Pt@COFs exhibit great pH-universal electrocatalytic activity toward HER, delivering superior performance across alkaline, acidic, and neutral media. Among these Pt@COFs, the heteroatom-rich Pt@TAzo-COF provide the best confinement effect for Pt immobilization, therefore Pt@TAzo-COF demonstrated the highest Pt loading and outperforming catalytic activity. This work provides a versatile design principle for engineering high-performance, stable electrocatalysts for advanced energy conversion under pH-universal condition.

Electronic Supplementary Material: Supplementary material (FTIR spectra, PXRD patterns, SEM & TEM images, XPS spectra, gas sorption isotherms, TGA, LSV curves et al.) is available in the online version of this article athttps://doi.org/10.26599/NR.2026.94909047.

Data availability

All data needed to support the conclusions in the paper are presented in the manuscript and the Electronic Supplementary

Material. Additional data related to this paper may be requested from the corresponding author upon request.

Acknowledgements

We are grateful for the financial support provided by the National Natural Science Foundation of Jilin Province (No. 20250101020JJ) and the National Natural Science Foundation of China (No. 22475036).

Declaration of competing interest

All the contributing authors reports no conflict of interests in this work.

Author contribution statement

J. H. L. and R. C. conducted materials synthesis, characterizations and electrocatalytic experiments. J. H. L. and C. Y. Z. performed theoretical calculations and characterizations. Y. X., S. H., and L. L. performed materials characterizations. J. L. L. and X. F. J. developed the concept and supervised the experiments. All of the authors contributed to the manuscript writing and approved the final manuscript.

Use of AI statement

None.

References

[1] Zhu, P.; Xiong, X.; Wang, D. S. Regulations of active moiety in single atom catalysts for electrochemical hydrogen evolution reaction. *Nano Res.* **2022**, *15*, 5792–5815.

[2] Zhang, H. H.; Fan, Y. P.; Guan, S. Y.; Cui, W. G.; Zhang, M. C.; Li, Z. L.; Dou, Y. H.; Yang, J. R.; Zhuang, Z. C.; Yuan, Z. L. et al. Research progress on Ti-based materials for MgH_2 hydrogen storage systems. *Compos. Funct. Mater.* **2025**, *1*, 20250201.

[3] Li, Z. C.; Huang, M. R.; Li, J.; Zhu, H. W. Large-scale, controllable synthesis of ultrathin platinum diselenide ribbons for efficient electrocatalytic hydrogen evolution. *Adv. Funct. Mater.* **2023**, *33*, 2300376.

[4] Li, X. Y.; Rong, H. P.; Zhang, J. T.; Wang, D. S.; Li, Y. D. Modulating the local coordination environment of single-atom catalysts for enhanced catalytic performance. *Nano Res.* **2020**, *13*, 1842–1855.

[5] Wu, Y. C.; Wei, W.; Yu, R. H.; Xia, L. X.; Hong, X. F.; Zhu, J. X.; Li, J. T.; Lv, L.; Chen, W.; Zhao, Y. et al. Anchoring sub-nanometer Pt clusters on crumpled paper-like MXene enables high hydrogen evolution mass activity. *Adv. Funct. Mater.* **2022**, *32*, 2110910.

[6] Han, Z.; Zhang, R. L.; Duan, J. J.; Wang, A. J.; Zhang, Q. L.; Huang, H.; Feng, J. J. Platinum-rhodium alloyed dendritic nanoassemblies: An all-pH efficient and stable electrocatalyst for hydrogen evolution reaction. *Int. J. Hydrogen Energy* **2020**, *45*, 6110–6119.

[7] Wan, X. K.; Wu, H. B.; Guan, B. Y.; Luan, D. Y.; Lou, X. W. Confining sub-nanometer Pt clusters in hollow mesoporous carbon spheres for boosting hydrogen evolution activity. *Adv. Mater.* **2020**, *32*, 1901349.

[8] Yang, Q.; Liu, H. X.; Yuan, P.; Jia, Y.; Zhuang, L. Z.; Zhang, H. W.; Yan, X. C.; Liu, G. H.; Zhao, Y. F.; Liu, J. Z. et al. Single carbon vacancy traps atomic platinum for hydrogen evolution catalysis. *J. Am. Chem. Soc.* **2022**, *144*, 2171–2178.

[9] Yang, X. R.; Ma, L.; Wang, S. Q.; Hu, X. Y.; Li, B.; Li, W.; Wang, D. S.; Dai, Z. H. Electrochemiluminescence-based multiplex immunoassays for multianalyte bioanalysis: Signal encoding strategies and analytical perspectives. *Electrochem. Commun.* **2026**, *186*, 108130.

[10] Li, S. L.; Xiao, Y.; Yan, H.; Yang, Y. T.; Tian, Y. Y.; Jing, X. F.; Zhu, G. S. Ultrafine platinum nanoparticles anchored in porous aromatic frameworks for efficient hydrogen evolution reaction. *Chem. Commun.* **2023**, *59*, 4766–4769.

[11] Xiao, Y.; Shi, Z. L.; Yan, H.; Li, J. H.; Han, S.; Yang, Y. T.; Jing, X. F. Elucidating host–guest interactions between phosphine-based porous aromatic frameworks and platinum for enhanced HER. *Chem. Commun.* **2025**, *61*, 16648–16651.

[12] Che, Y.; Chen, D. S.; Wang, B.; Li, M. Y.; Zhao, Y. Y.; Zhu, G. S.; Xing, H. Z. Site-specific asymmetric coordination engineering in defective metal-organic frameworks stabilizes Cu(I) active sites for selective CO_2-to-methanol photocatalysis. *J. Am. Chem. Soc.* **2026**, *148*, 5764–5773.

[13] Guo, Y. J.; Liu, Z. Y.; Zhou, D. Y.; Zhang, M. Y.; Zhang, Y.; Li, R. Z.; Liu, S. L.; Wang, D. S.; Dai, Z. H. Competition and synergistic effects of Ru-based single-atom and cluster catalysts in electrocatalytic reactions. *Sci. China Mater.* **2024**, *67*, 1706–1720.

[14] Salah, A.; Ren, H. D.; Yu, F. Y.; Al-Ansi, N.; Lang, Z. L.; Li, Y. G.; Wang, Y. H.; Tan, H. Q. Boron carbide supported ultra-small ruthenium nanoparticles with high-performance for hydrogen and chlor-alkali Co-production. *Adv. Energy Mater.* **2026**, *16*, e06175.

[15] Zhang, Y.; Wan, W. K.; Peng, Y. D.; Guo, Y. J.; Zhou, J. L.; Wang, S. C.; Yuan, J. Y.; Liao, Y. R.; Liu, L. S.; Zhang, Y. F. et al. Corrosion-resistant single-atom catalysts for direct seawater electrolysis. *Natl. Sci. Rev.* **2025**, *12*, nwaf060.

[16] Maruta, Y.; Ashitani, H.; Kawaguchi, S.; Ina, T.; Sakata, O.; Kubota, Y.; Yamamoto, T.; Toriyama, T.; Murakami, Y.; Mukoyoshi, M. et al. Revealing dynamic structural changes in platinum-group-metal nanoparticles during the catalytic hydrogen evolution reaction. *J. Am. Chem. Soc.* **2025**, *147*, 36934–36939.

[17] Li, J. H.; Jing, X. F.; Li, S. L.; Ma, L. N.; Yang, Y. T.; Han, S.; Jia, J. T.; Yavuz, C. T.; Zhu, G. S. Binder-free Pt/PAF membrane electrodes for durable, high-current-density hydrogen evolution. *Matter* **2025**, *8*, 102047.

[18] Wang, Y.; Chen, Y. G.; Nan, C. Y.; Li, L. L.; Wang, D. S.; Peng, Q.; Li, Y. D. Phase-transfer interface promoted corrosion from $PtNi_{10}$ nanoctahedra to Pt_4Ni nanoframes. *Nano Res.* **2015**, *8*, 140–155.

[19] Wang, S. W.; Wang, L. G.; Zhou, X. D.; Fang, J. J.; Deng, C.; Wang, D. S. Design principles of single-atom catalysts anchored over porous materials for green catalysis and conversion. *Nano Res.* **2025**, *18*, 94907137.

[20] Wang, C.; Zang, H.; Liu, C. J.; Wang, J. H.; Kuai, L.; Geng, B. Y. Synergistic acid hydrogen evolution of neighboring Pt single atoms and clusters: Understanding their superior activity and mechanism. *Inorg. Chem.* **2023**, *62*, 6856–6863.

[21] Zhou, W.; Deng, W. Q.; Lu, X. Metallosalen covalent organic frameworks for heterogeneous catalysis. *Interd. Mater.* **2024**, *3*, 87–112.

[22] Cai, H. Z.; Wang, L.; Liu, W.; Zhang, X.; Chen, B. B.; Mao, P. Y.; Fang, J. C.; Gao, R.; Shi, C. Re-dispersion of platinum from CNTs substrate to α-MoC_{1-x} to boost the hydrogen evolution reaction. *Small* **2023**, *19*, 2207146.

[23] Zhang, Y. F.; He, Z. D.; Yang, C.; Cao, P. P.; Ma, Q.; Liu, H.; Heng, X. Y.; Gu, T. H.; Shi, J. Q.; Mu, X. Q. et al. Interfacial microenvironment regulation strategies for industrial-scale hydrogen evolution. *EnergyChem* **2026**, *8*, 100189.

[24] Tan, Y. S.; Feng, J. R.; Dong, H. B.; Liu, L. X.; Zhao, S. Y.; Lai, F. L.; Liu, T. X.; Bai, Y.; Parkin, I. P.; He, G. J. The edge effects boosting hydrogen evolution performance of platinum/transition bimetallic phosphide hybrid electrocatalysts. *Adv. Funct. Mater.* **2023**, *33*, 2209967.

[25] Xiong, J. X.; An, Q.; Xiang, H.; Zhou, Y.; Zhang, Y.; Chen, W. J.; Ren, B. X.; Wang, S. X.; Bai, H. P.; Guo, H. et al. Topology

engineering of COFs via localized 1D-2D unit interconnection to facilitate interfacial electron transfer for efficient gold recovery from e-waste leachates. *Chem. Sci.* **2026**, *17*, 436–447.

[26] Zhao, Y.; Chen, Y. Q.; Yu, Y.; Xing, G. L.; Chen, L. F.; Xia, F.; Ben, T. Symmetry-shearing chemistry enabled interdigitated 2D covalent organic frameworks with interlayer mortise-and-Tenon interlocks for efficient photocatalytic CO_2 fixation. *J. Am. Chem. Soc.* **2025**, *147*, 40319–40330.

[27] Yin, L. Y.; Guo, X. Y.; Hu, J. F.; Yan, K. M.; Liu, L.; Shi, X. Y.; Cui, F. C.; Zhu, G. S.; Zhang, N. Strategic nitrogen site alignment in covalent organic frameworks for enhanced performance in aqueous zinc-iodide batteries. *Angew. Chem., Int. Ed.* **2025**, *64*, e202423265.

[28] Tan, Y. J.; Sun, C. L.; Han, G. K.; Qian, Z. Y.; Gu, Y.; Ye, N.; Lin, Z.; Huang, Q. Z.; Liu, F.; Wei, C. Z. et al. Neutral electrosynthesis of methane from diluted CO_2 on dense Cu sites embedded covalent organic frameworks. *J. Am. Chem. Soc.* **2026**, *148*, 3327–3335.

[29] Zhang, J. Y.; Wan, Z. Q.; Bu, X. M.; Fan, H. X.; Lou, H. W.; Gao, J.; Wen, D.; Gao, W. Electronic interaction enables Pt nanoparticles on N-doped porous carbon aerogel as efficient electrocatalysts for alkaline hydrogen evolution reaction. *Small* **2025**, *21*, e06453.

[30] Wang, Y.; Ma, F. Y.; Zhang, G. Q.; Zhang, J. W.; Zhao, H.; Dong, Y. M.; Wang, D. S. Precise synthesis of dual atom sites for electrocatalysis. *Nano Res.* **2024**, *17*, 9397–9427.

[31] Yuan, H.; Chen, P. F.; Li, X.; Xu, X. X.; Qian, W.; Zhang, H. Z.; Wang, Z.; Fu, H. Q.; Wang, D. S.; He, D. P. Scalable fiber-skeleton-reinforced graphene-assembled films enabling wash-durable wearable heating. *Nano Res.* **2026**, *19*, 94908671.

[32] Zheng, X. H.; Liu, H.; Cui, J. L.; Guo, Y. M.; Xu, H. Z.; Zhang, Z. J.; Zhang, J. M.; Zhao, Y. J. Solvent-directed *in situ* stacking modulation of 2D covalent organic frameworks for selective separation of xylene isomers. *Angew. Chem.* **2026**, *138*, e19150.

[33] Weng, W. J.; Guo, J. Chiral covalent organic framework films with enhanced photoelectrical performances. *J. Am. Chem. Soc.* **2024**, *146*, 13201–13209.

[34] Ma, X. K.; Han, W. K.; Zhu, H. S.; He, T.; Wang, Z. F.; Zhou, W.; Wu, X. S.; Ma, Y. X.; Huang, Z. Y.; Zhao, Y. et al. Enabling rotated stacking displacement in two-dimensional covalent organic frameworks via interlayer electrostatic repulsion. *Angew. Chem., Int. Ed.* **2026**, *65*, e24407.

[35] Tan, J.; Weng, W. J.; Zhu, J. Y.; Liu, S. J.; Xu, J.; An, S. H.; Wang, C. C.; Guo, J. A phosphine-amine-linked covalent organic framework with staggered stacking structure for lithium-ion conduction. *Angew. Chem., Int. Ed.* **2023**, *62*, e202310972.

[36] Huang, W.; Yuan, H. T.; Yang, H. S.; Ma, X. M.; Huang, S. Y.; Zhang, H. J.; Huang, S. M.; Chen, G. S.; Ouyang, G. F. Green synthesis of stable hybrid biocatalyst using a hydrogen-bonded, π–π-stacking supramolecular assembly for electrochemical immunosensor. *Nat. Commun.* **2023**, *14*, 3644.

[37] Yao, W. K.; Zhou, G. B.; Liu, T.; Yuan, Y. H.; Wang, H.; Wang, N. Defect engineering activates pyrene-based covalent organic frameworks for efficient photocatalytic uranium capture. *Adv. Sci.* **2026**, *13*, e18948.

[38] Javed, O.; Gong, S. T.; Zhang, X. L.; Han, L.; Zhang, H. Y.; Zhang, B. N.; Jin, Q.; Yang, M.; Yan, X. M.; He, G. H. et al. Pyrene containing, highly conductive and robust poly (aryl piperidinium) anion exchange membranes for fuel cell applications. *J. Membr. Sci.* **2025**, *725*, 124028.

[39] Kresse, G.; Furthmüller, J. Efficient iterative schemes for *ab initio* total-energy calculations using a plane-wave basis set. *Phys. Rev. B* **1996**, *54*, 11169–11186.

[40] Kresse, G.; Furthmüller, J. Efficiency of *ab-initio* total energy calculations for metals and semiconductors using a plane-wave basis set. *Comput. Mater. Sci.* **1996**, *6*, 15–50.

[41] Perdew, J. P.; Burke, K.; Ernzerhof, M. Generalized gradient approximation made simple. *Phys. Rev. Lett.* **1996**, *77*, 3865–3868.

[42] Grimme, S.; Antony, J.; Ehrlich, S.; Krieg, H. A consistent and accurate *ab initio* parametrization of density functional dispersion correction (DFT-D) for the 94 elements H–Pu. *J. Chem. Phys.* **2010**, *132*, 154104.

[43] Henkelman, G.; Uberuaga, B. P.; Jónsson, H. A climbing image nudged elastic band method for finding saddle points and minimum energy paths. *J. Chem. Phys.* **2000**, *113*, 9901–9904.